Fragmentation dynamics of single agglomerate-to-wall impaction

A. Lowe[1], G. Singh[1], H-K. Chan [2], A.R. Masri [1], S. Cheng[3], and A. Kourmatzis[1*],

1: School of Aerospace, Mechanical and Mechatronic Engineering, The University of Sydney, NSW, 2006 Australia

2: Advanced Drug Delivery Group, School of Pharmacy, The University of Sydney, NSW, 2006 Australia.

3: School of Engineering, Macquarie University, NSW, 2109 Australia.

* agisilaos.kourmatzis@sydney.edu.au

Abstract

The de-agglomeration characteristics of single agglomerate-wall impaction are examined using high-resolution shadowgraph imaging. Experiments are performed to investigate the effects of constituent particle size (D_{50} from 3-7 μm) and air velocity on the individual size and velocity of de-agglomerated fragments at conditions relevant to dry powder inhalation systems. De-agglomerated fragment area and trajectories were used to differentiate between pseudo-elastic and inelastic collisions during de-agglomeration. Advanced image processing techniques have enabled provision of joint population distributions of fragment area and aspect ratio, which identify a bimodal dispersion of fragments during de-agglomeration. The bimodality is destroyed with increasing air velocity and also generally diminishes with time after impact. The experiment presented forms a platform for the detailed quantitative characterisation of de-agglomeration behaviour and can be useful towards the development and validation of related computational models for pharmaceutical dry powder inhalers.

Keywords

Dry powder inhalers, pharmaceutical powders, de-agglomeration

1. Introduction

Treatment of respiratory diseases rely heavily on the performance of pulmonary drug delivery systems, such as dry powder inhalers (DPI) [1, 2]. In treatments ranging from chronic obstructive pulmonary disease (COPD), asthma and emphysema [3, 4], delivery of the prescribed drug was most effective when administered uniformly over a wide coverage area, and deep in the lung cavity; resulting in enhanced absorption and therapeutic onset [4]. DPIs are commonly used to achieve this due to their theoretical ease-of-use (portability, low cost, simple functionality), lack of additives (propellants) and physical stability (reduced chemical degradation when using dry solid drug particles), when compared to metered dose inhaler or nebulizer equipment [1, 5]. Despite these advantages, many DPIs suffer from poor dispersion [6], resulting in delivered dose loads ranging from 40% to as low as 12% in practice [6]. Several key factors contribute to lung deposition inconsistency, including device performance, drug powder formulation, and inhalation flow [7]. In DPIs, flow and dispersion are driven by the patient, as opposed to metered dose inhaler devices which rely on propellants. As a result, insufficient de-agglomeration of fine drug particles can be observed in DPIs when there is insufficient impaction. Therefore, understanding the interaction of these agglomerates with the inner geometry of DPIs becomes crucial, although quantitative characterisation of these processes remains limited.

In practice, dry drug powders are packed into capsules, reservoir dispensers or sealed blisters [8] that tend to agglomerate before they are loaded into DPIs. Although the method of metering the drug may vary, the principal function of the DPI is the same; powder is fluidised in a flow given adequate residence time, and is delivered to the patient in a dispersed stream at the mouthpiece. In pure active pharmaceutical ingredient (API) applications, agglomerates interact with the internal ge-

ometry of the inhaler (walls, grids, cyclone paths) and other agglomerates. The delivered stream is typically poly-disperse; populated by both single and grouped fragments of constituent drug particles. The physical forces acting between particles is a complex combination of van der Waals, capillary and electrostatic forces [9, 10, 11] with the contribution of each of these forces being dependant on environmental factors such as temperature, relative humidity; and particle properties such as surface energy, static charge, mechanical strength, shape and particle size distribution [9, 10, 11]. The specific influence of each of these forces and their dependence on physical and environmental factors add to the complexity of theoretically characterising de-agglomeration; especially since both single particles and fragments can be irregular in shape [12]. Whether agglomerates are naturally or intentionally formed; it has been shown in many studies that increased in-homogeneity in channel flows by inducing turbulence can be beneficial. Localised turbulence intensity can potentially increase flowability and dose accuracy in DPIs, by consistently delivering more fine API particles deeper in the airway [13, 14, 15]. An understanding of agglomerate-wall and agglomerate-agglomerate interactions are therefore necessary for both physical insight and predictive models in practical applications.

Of critical importance to the de-agglomeration process, is the generation of particles at an inhalable size (less than $5\boldsymbol{\mu m}$). Peak inspiratory flow rates range from 20 - 120 L/min (depending on age and disease severity) and it must be ensured that these flows, combined with device attributes, are sufficient to create fine particles. De-agglomeration induced by the rapid deceleration of the agglomerate during impact is therefore a process of ubiquitous relevance to DPIs [16]. For this reason, precisely positioned DPI cyclone flow paths, impaction grids and walls are used to enhance fluid dynamic shear stresses and direct impaction forces [14, 13, 17, 5]. Characterising these fluid forces, particle-particle and particle-wall interactions are necessary to optimise DPI dispersion mechanisms [18, 19].

The impact of several design parameters in DPIs on de-agglomeration have been studied previously, such as air inlet size, air flow rate, mouthpiece length and grid structure [20, 21, 22]. These studies focused on investigating specific design parameters or powder formulation effects on the particle laden flow inside commercial DPI replicas by using PIV techniques. For example, Han et al. [23] mapped the flowfield using PIV inside the mouthpiece of a Spiros inhaler to study its specific drug dispersion mechanism. In that inhaler, the impaction mechanism was identified as a dominant component and affected the rate of drug particle emission from the dispersion chamber in the first 2 seconds of operation. It was concluded that reducing the particle wall collisions would reduce drug loss due to deposition in the DPI. Kou et al. [24] proposed that the drag force, impaction and particle-particle collisions are dominant dispersion mechanisms common to all DPIs after performing a PIV and direct flow visualisation campaign in a Rotahaler. Using similar experimental techniques, the fluidisation of lactose powder in a Nexthaler has been observed as a highly turbulent rotating flow structure at the DPI outlet [24]. This flow pattern resulted in enhanced wall impaction and drug de-agglomeration where the time scale of bulk powder evacuation from the device was approximately 100-200ms. Voss et al. [17] used optical techniques to study powder impaction and concluded that turbulence was an effective de-agglomeration mechanism. Tong et al. [25, 13] used theoretical methods and experimental analysis to show that agglomerate experience significant plastic deformation on impact. Similarly, Thornton et al. [26] correlated higher single agglomerate impact velocity with greater local fracture and degree of wall residue. This is supported by the review of applied discrete element methods (DEM) and CFD studies on de-agglomeration by Yang et al. [27, 13, 28], who concluded that impact velocity played a dominant role in increasing the dispersion ratio.

Despite significant efforts, there remains a critical lack of knowledge on the in-

teractions of agglomerates with other agglomerates and particles, solid boundaries, and air, to form the dispersed phase. This requires spatio-temporally resolved imaging systems to capture particle-flow interactions and characterise particle dispersion dynamics during fragmentation. This study aims to characterise the fragmentation process during single agglomerate-wall interactions, under flow conditions which are relevant to pharmaceutical DPI flows, using high-speed microscopic backlit imaging combined with advanced in-house image processing techniques. High-speed microscopic backlit imaging is capable of quantifying non-spherical particle dynamics in DPIs and is widely used in the characterisation of spray jets and atomizers [29, 30]. Although PIV has been used to characterise flow-fields in DPIs, it lacks the ability to differentiate between particle size bands and particle shapes. In this paper, the dispersion characteristics of single agglomerates are studied as a function of powder formulation and inhalation flow. Single agglomerate-wall interactions are quantified in detail, where the effects of constituent particle morphology and air flow are isolated and varied.

The first section of this paper introduces the single agglomerate impaction channel with a detailed summary of the flow conditions, imaging set up and material properties. This is followed by a detailed experimental study of single agglomerate-wall impacts for selected cases of mannitol using high speed microscopic backlit imaging. A parametric study comparing the effects of constituent particle size and air flow is used to analyse their global effects on fragmentation, wall deposition and particle trajectories and velocities. Finally, population distributions of size and shape are presented at discrete temporal locations of interest.

2. Materials and Methods

2.1. Experimental Setup-Impaction Channel

The impaction channel, shown schematically in Figure 1, uses air flow to accelerate single agglomerates vertically downward onto a flat horizontal surface. This allows direct control of the magnitude of deceleration of the agglomerate on impact. The global difference of induced stress over the forces holding the agglomerate together (a mixture of Van der Walls, capillary and electrostatic forces) can be intensified and scaled to characterise de-agglomeration behaviour. The applied air flowrate incrementally ranges between two extremes; zero (purely gravitational free-fall) and 100 slpm, to mimic realistic physiological inhalation conditions. The square acrylic channel is 700 mm in length and the interior cross-sectional dimensions are 10 x 10 mm. Air is delivered from the top section through a mass flow controller and the velocity profile in the channel is assumed parabolic. For repeatable agglomerate delivery (refer to Detail: A in Figure 1), a threaded perspex bolt was machined flush with the interior wall of the channel as to not perturb the flow. A hole 2 mm in diameter was drilled through the centre of the bolt and is located 500 mm downstream from the top of the channel. A single agglomerate is physically inserted into the vertical downward cross-flow at an initial vertical velocity of zero and horizontal velocity of 1 mm/min. This is achieved using a linear actuator (Actuonix L16-R Servo), where the actuator trigger is synced with the acquisiton window of the imaging setup. The relative distance between this point of release of the single agglomerate and a flat horizontal quartz plate onto which it impacts can be adjusted and is set to 150 mm.

2.2. Imaging Setup

Microscopic backlit imaging (Figure 1) was conducted at a repetition rate of 10 kHz using a 300 Watt double-pulsed diode laser (Oxford Lasers Firefly) as an illumination source. The 808-810 nm beam is guided sequentially through a single 1" opal glass diffuser and a 2" collimating lens, which removes coherence from the beam and also provides a uniform illumination source. On the collection side, a high-speed CCD camera (Photron FASTCAM AX100, 16GB) and long distance microscope (Questar QM-100) are used to provide a field of view (FOV) of width 2.8 mm and height 1.87 mm with a 768 × 512 pixel resolution; 5000 images are collected per impact repetition for quantitative characterisation. The camera and laser are synchronized in frame-straddling mode, such that two laser pulses are positioned on sequential CCD frames. Each of the two exposures are recorded on separate frames, followed by analysis based on cross-correlation of the two frames. Recording on separate frames preserves the time sequence of the pulses so no directional ambiguity occurs. Cross-correlation processing provides improved dynamic range for velocity compared with auto-correlation of double exposures. Here, to achieve a 10K frames-per-second rate, the double pulse laser is set to ext/2 +ve trigger mode with a 50 ms separation, 125 ms delay and 0.24 ms duration. In order to extract quantitative information from such images, images are binarized following a careful choice of pixel threshold. Binarization enables identification of the interface between individual powder fragments and air. The effect of pixel threshold on the uncertainty in the results has been extensively studied in previous work [29, 30, 31], with estimates of Sauter mean Diameter agreeing to within 5-10**%** with phase Doppler anemometry. This calibration method chosen here limits the optical spatial resolution to 3.65 $\boldsymbol{\mu}$m per pixel. With 4x4 binning, this results in a minimum measurable fragment size of approximately 15 $\boldsymbol{\mu}$m. Therefore in this contribution we focus largely on fragments generated post-impact, as opposed to analysis of fine particles. It is also important

to understand that out-of-plane motion remains a limitation for single viewing angles and this can only be eliminated through the use of multi-angle imaging which is forthcoming. Similarly, a full consideration of impact de-agglomeration asymmetry due to the depth of field of the lens can only be fully accounted for using multiple viewing angles. Notwithstanding these limitations, the calibration technique used here employed a binarization intensity threshold (with respect to the background) that varies from 35-45% and this is in excellent agreement with recommended background thresholds used to binarize similar two-phase flow measurements in turbulent sprays for the same lens and camera layout [29, 30].

The velocity of the particles is obtained by tracking them in subsequent images, using a PTV technique as discussed elsewhere [29]. The uncertainty in velocity is limited to 10-15**%**. It is also important to understand that out-of-plane motion remains a limitation for single viewing angles and this can only be eliminated through the use of multi-angle imaging which is forthcoming. Similarly, a full consideration of impact de-agglomeration asymmetry due to the depth of field of the lens can only be fully accounted for using multiple viewing angles. Notwithstanding these limitations, the calibration technique used here employed a binarization intensity threshold (with respect to the background) that varies from 35-45% and this is in excellent agreement with recommended background thresholds used to binarize similar two-phase flow measurements in turbulent sprays for the same lens and camera layout [29, 30].

2.3. Constituent Particles and Agglomerates

2.3.1. Powder Properties

Raw mannitol (Pearlitol 160C) was obtained from Rocquette Fréres France and was used as the only constituent particle ingredient for agglomerates. Spherical

mannitol particles were produced via a spray dryer (Buchi 290, Flawil, Switzerland) with an inlet air temperature of 140°C, aspiration set at max 38 m^3/h and atomising air rate of 800 NL/h (refer to conditions stated in Table I). Three constituent particle size samples of mannitol powder, named M3, M5 and M7 were prepared with approximate D_{50} set to 3, 5 and 7μm respectively. The direct control of constituent particle population size was achieved by varying the feed concentration of raw mannitol to de-ionised water (>2 MΩm resistivitiy at 25°C, obtained from the Modulab Type II Deionization System, Continental Water System) from 4-18 mg/mL and feed rate into the atomiser set to 3.8-8 mL/min. **Mannitol particles were used in this study as constituent particles due to ease of agglomerate rolling. Creating agglomerates of a nearly consistent size proved challenging with larger carrier particles of lactose, and hence this was not pursued**.

The particle size distributions of the spray-dried powders were determined on a wet disperser (Hydro SM, Malvern, Worcs, UK) connecting to a laser diffractometer (Mastersizer 2000, Malvern, Worcs, UK). The refractive indices of mannitol used were 1.520 and 0.100 for the real and imaginary components, respectively, and the dispersing medium chloroform was 1.444. Chloroform was supplied by Biolab Australia and plastic syringes (50 mL, 29.1 mm i.d.) were supplied from Livingstone, Australia. The population size distributions by volume for the three powders are presented in Figure 2, displaying the cumulative volume diameters: D_{10}, D_{50} and D_{90} for reference. The half-width of these distributions is approximately 5 μm for all cases. From this point forward, the mannitol powder samples with D_{50} measurements of 2.92, 4.96 and 6.77 μm will be referred to hereon as the 3, 5 and 7 μm mannitol powders respectively (M3, M5 and M7).

2.3.2. Single Agglomerate Strength

For this particular dataset, single agglomerates comprising of each constituent particle were rolled to an approximate diameter of D = 1.2-1.5 mm using a roller mixer (Ratek Instruments, BTR5). A cylindrical stainless steel container with a 1" interior diameter and 2" interior length was filled with constituent particle powder to a third of its capacity and rolled for 10 minutes at maximum 60 rpm with tilt angle of 3.5 degrees from horizontal. Agglomerates with diameters 1.2 to 1.5 mm were separated from the rolled product using a stainless steel staged sieve, where the upper and lower stages were CNC machined with hole sizes 1.2 and 1.5 mm with 0.01 mm tolerance. The agglomerate size variance is due to the fragility of the mannitol material during rolling, sieving and handling. All spray dried powders and agglomerates were stored in a desiccator over silica gel to provide 15-20% relative uniform humidity until use. **The density of the agglomerates was also determined by measuring their approximate volume under a microscope, and weighing at least 3 agglomerates from the 3, 5, and 7um mannitol powders. As these measurements were done using a single planar view to determine an agglomerate diameter-they are only an approximation**.

A universal mechanical testing instrument (Electromechanical Intron), with a low-load of 0.5 kN, was used to apply compression stress tests to characterise single agglomerates fracture strength. In these tests, a single agglomerate is placed in a central loading cell between two plates, the base plate being stationary. Before each iteration, the top plate is aligned to the top surface of the agglomerate i.e. the first vertical point of feedback. This initial displacement between the plates is used to normalise the deformation during the compression and calculate the strain. The stress is approximated as the feedback force from the loading cell divided by a cross-sectional circular area, matching the agglomerate diameter measured with a digital caliper. Each compression test is completed when the spacing between the loading

cell plates is 0.1 mm. The pseudo-average stress and strain curves ($\boldsymbol{\delta}$ vs. $\boldsymbol{\epsilon}$) are plotted for single agglomerates of approximate diameter 1.2-1.5 mm in Figure 3. Here, we compare single agglomerates composed of mannitol powder with $D_{\mathbf{50}}$ = 3, 5 and 7 $\boldsymbol{\mu}$m for five repetitions per case. It is clear that the onset of fracture initiates earlier for agglomerates composed of larger mannitol powder. The initial stress feedback of approximately 10 kPa is greatest for the M3 case, and reduces to 4 kPa and 2 kPa for M5 and M7 respectively. As the strain is increased to 30% all cases approach near zero stress. Assuming uniform material continuity, as particle size decreases, total contact area between particles in an agglomerate increase, causing an increase in the total strength of the agglomerate. However, it is important to note that there is some variance between the results for similar agglomerates due to the analysed first fracture point being related to agglomerate shape and continuity of the material.

3. Results: Temporally resolved high-speed imaging

Prior to presenting detailed quantitative results on the fragmentation characteristics of the single agglomerate-wall impaction events, representative snapshots of de-agglomeration are first shown. Figure 4 displays 'free-fall' case M3-0 alongside the post-processed images; time, t = 0 ms is defined as the first instance the surface of the 'original' agglomerate contacts the impaction plate. In each sequential frame, a 'parent' agglomerate is defined as the largest fragment displaced from the impact plate, 'daughter' fragments are any subsequent displaced fragment, and wall deposition is defined as the fragments still in contact with the plate after t = 0 ms. Instantaneous blocked area is defined as the total 2D blocked area of the 'parent', 'daughter' and wall deposition fragments at time, t. In general, as the original agglomerate collides (pseudo-elastically or inelastically) with the impaction plate, a relatively large population of 'daughter' fragments are displaced from the 'parent' agglomerate in the first 10 ms. The 'parent' agglomerate visually rotates and gener-

ates a wake with which the majority of the 'daughter' fragments interact. This interaction is illustrated by a rolling cloud of daughter fragments at 24 and 40 ms, until the steady-state condition (t = SS) is reached by 150 ms.

Figure 5 compares the effects of constituent particle size and air velocity (note the time step increases for greater air velocity) and the corresponding initial conditions are tabulated in Table II for reference. The time sequence progresses from left to right until the steady-state condition is reached in the final frame. Given sufficient residence time, the 'parent' and 'daughter' fragments leave the field-of-view, the fragments attached to the impaction plate remain unchanged and the final wall deposition is calculated (defined at t = 150, 100 and 50 ms for U_j = 0, 10 and 17 m/s respectively, see final right column of Figure 5). The naming methodology adopted in Table II is employed here; for example, case M5-17 is for an agglomerate composed of mannitol constituent particle size D_{50} = 5 μm, where the initial air velocity is 17 m/s. Cases are grouped from M3-M7: for air velocity U_j = 0 m/s (Figure 5 row 1-3), U_j = 10 m/s (Figure 5 row 4-6) and U_j = 17 m/s (Figure 5 row 7-9). In each group, the air velocity is constant and comparisons are made for three constituent particle sizes, D_{50}, 3 μm (top), 5μm (middle) and 7 μm (bottom).

3.1. Free-fall case

Comparing the free-fall cases (U_j = 0 m/s) M3-0 to M7-0 in Figure 5, the degree of breakup increases with constituent particle size. Referring to Figure 3, increasing the constituent particle size relates to lesser gradient for the pseudo-average stress and strain relationship. For a carrier velocity of zero, comparing images from 0 - 10 ms, increasing in constituent particle size from 3 to 7 μm results in a wider size range of fragments breaking off the 'parent' agglomerate during de-agglomeration. The rate and magnitude of the pseudo-elastic collision reduces for increased constituent particle size. This is evident through the fast rebound of the 'parent' agglomerate from

the plate in the 0 - 2 ms interval for case M3-0, evident through the 4-6 ms interval for case M5-0, and evident through the lack of rebound for case M7-0. It follows that the vertical displacement between the plate and the 'parent' agglomerate also reduces as $D_{\mathbf{50}}$ increases. Distinctly for 7 $\boldsymbol{\mu}$m cases, the original agglomerate does not breakup on impact but rather adheres to the plate after spreading across it.

3.2. With positive air velocity

The aforementioned trends discussed in section **3.1** are also consistent as the air velocity increased incrementally to 10 m/s (cases M3-10 to M7-10) and 17 m/s (cases M3-17 to M7-17). An additional observation is the increase in momentum of the single agglomerate before impaction which increases de-agglomeration, resulting in greater magnitude of dispersion and further expansion of the size range of fragments that appear. This is most visibly clear when comparing a time instance of 2 - 4 ms in cases M3-0, M3-10 and M3-17 for the 3$\boldsymbol{\mu}$m case. The size distribution of fragments that break off the 'parent' agglomerate is smaller for the free-fall case and the velocity at which these fragments disperse away from the 'parent' agglomerate appear faster as well. The one discrepancy is the pseudo-elastic behaviour of the 'parent' agglomerate as the air velocity increases past 10 m/s for cases M5 and M7. For these higher velocity conditions, there is more significant mixing surrounding the agglomerate due to the airflow impinging on to the plate. The transfer of momentum from gas to fragments due to increased fragmentation results in a bounce of lesser magnitude for the 'parent' agglomerate with a subsequent increased spanwise spread of 'daughter' fragments. In every case, the degree of wall deposition increases with constituent particle size and air velocity up to the provided time instances. These observations in the images have been statistically verified in the next section.

4. De-agglomeration characterisation for single impacts

This section provides extracted size, shape and trajectory statistics used to quantitatively characterize single agglomerate-wall interactions on impact by varying constituent particle size and air velocity.

4.1. Global evolution of fragments

The global de-agglomeration process is characterised by providing averaged statistics from N = 25 discrete repetitions for all cases in Table II. Figure 6 displays the temporal development of a) normalized area (left column) and b) one standard deviation (right column) for air velocity 0 m/s (top, free-fall), 10 m/s (middle) and 17 m/s (bottom). The results demonstrate a detailed quantitative account of agglomerate-wall fragment evolution based on ensemble averaging from multiple repetitions.

Each plot compares the trend for the three constituent particle sizes up to 10 ms after the first contact between the agglomerate and the plate. Referring to Figure 4, the normalized area is defined as the total sum of blocked 2D areas in each image frame divided by the total number of samples, N ($\sum_{t>0}^{\infty} \boldsymbol{A_t}$: 'parent', 'daughter' fragments and wall deposition as defined in Section 3 at time, t > 0 ms) normalized by the blocked area of the original agglomerate, $\boldsymbol{A_{t=0}}$. At t = 0 ms, all cases for normalized area change (left column, Figure 6a) have a value of 1. One standard deviation for the total population of blocked 2D areas ($\boldsymbol{\delta_{A_t}}$) present in each timestep is used to describe the temporal variance in population size distribution.

For the normalized area change (Figure 6, top row), case M3-0 (free-fall, $\mathbf{D_{50}}$ = 3$\boldsymbol{\mu}$m) starts at a value of 1 (0% difference between the computed blocked area and that of the original agglomerate) at t = 0 ms and decreases linearly after approximately t = 4 ms. However, the averaged blocked area for both cases M5-0 and M7-0

(D_{50} = 5 and 7 μm respectively) increase mildly by 10% across this acquisition window. This difference is due to the 'parent' agglomerate leaving the field of view due to a largely pseudo-elastic collision for D_{50} = 3μm and transitioning to show behaviour where fracture of the agglomerates occur with increasing constituent particle size. While momentum of the system is conserved in these inelastic collisions, kinetic energy has largely been transferred to material breakup of the 'parent' agglomerate (increase in the number and intensity of fracture).

When 10 m/s of air is applied (Figure 6, middle column), the aforementioned trends with constituent particle size remain, however the degree of dispersion is greater. Case M3-10 starts to decay sooner than case M3-0 (free-fall) at 2 ms due to greater initial momentum. However, the 'parent' agglomerate remains largely intact as the normalized area does not increase more than 20%. In contrast, both cases M5-10 and M7-10 increase to a peak of 60% average blocked area at 4 ms due to greater dispersion of fragments and decay at the same rate as the 3 μm case (M3-10). It is important to note here that the original agglomerate compresses by 20% in the first 0.2 ms but does not rupture significantly.

Finally for U_j = 17 m/s, all agglomerates including the 3μm case fracture irrespective of constituent particle size. The M3-17 increases by 50% to a peak averaged blocked area at close to 2 ms after impact and the 5μm case (M5-17) increases by 85% by approx by 3 ms. The main difference occurs for M7-17 in the first 0.2 ms during impact, where the average blocked area reduces rapidly by 50%. This behaviour was mild for the U_j = 10 m/s cases but the magnitude of inelasticity in the U_j = 17 m/s collision is so significant at D_{50} = 7μm, that the direction of momentum does not act to oppose the flow but is transferred radially. This results in a 'splash" impact where the agglomerate does not rebound off the plate, the averaged blocked area initially drops rapidly and the fragments are eventually swept up by the air to reach a peak blocked area at 3 ms. The decay rate after the peak normalized area is

consistent irrespective of constituent particle size and increases with the magnitude of U_j.

The standard deviation of fragments at each time interval, $\boldsymbol{\delta}_{A_t}$, is displayed in Figure 6b (right column) for different carrier velocities. It is important to note that there is a population bias in the calculation towards fragments compared to the single 'parent' agglomerate in each image. This means that for any de-agglomeration event, the standard deviation will decrease over time as the fragments become more dispersed in the field of view. For the free-fall case, the standard deviation of fragment sizes increases with constituent particle size as is clear when comparing the 3 and 5 $\boldsymbol{\mu}$m cases M3-0 and M5-0 respectively. It was noted from the images that M7-0 is not well dispersed because the 'parent' agglomerate does not leave the impaction plate and this results in a lower standard deviation value. The standard deviation of blocked areas shows an overall increase as the air velocity is applied to the 3$\boldsymbol{\mu}$m cases, this is in contrast to an overall decrease for the 5 and 7 $\boldsymbol{\mu}$m cases which indicates a more homogeneous distribution of fragments as the agglomerate collision becomes increasingly inelastic.

For case by case comparisons, the standard deviation of the instantaneous normalized area change $\boldsymbol{\delta}_{\overline{A_t}}$ is presented in Figure 7. This repetition test shows the variance in results due to agglomerate disparities that are not physically controllable i.e. pre-existing fracture sizes, locations, agglomerate shape and point of load. For the free-fall case, the standard deviation of normalized area change is constant from impact to 5 ms at which point the variance in the 3 $\boldsymbol{\mu}$m case (M3-0) begins to increase. This variance is due the vertical trajectory of the agglomerate after the pseudo-elastic collision with the plate, which is highly dependent on shape. Intuitively for a perfectly spherical agglomerate the collision would result in trajectory normal to the plate. Introducing the air provides a degree of directional modulation in the particle laden flow after de-agglomeration and decreases the overall variance

between cases due to constituent particle size. The main disparities between repetitions occur at the 4 - 6 ms time interval for U_j = 10 m/s (M3-10 to M7-10) and 1-3 ms time interval for U_j = 17 m/s (M3-17 to M7-17). Information such as this is rarely considered when modelling agglomerate interactions, and is critical when comparing models to experiment.

4.1.1. Centroid Trajectory Tracking

Figure 8 displays the a) mean centroid axial trajectory, Y_t/N and b) one standard deviation, δY_t for the 'parent' agglomerate in the acquisition field of view. In contrast to the previous results shown, this provides the temporal evolution of the single largest mannitol fragment only.

For the free-fall cases (top row), increasing the constituent particle size from 3-7 μm transitions the collision behaviour from pseudo-elastic (M3-0) to inelastic (M5-0 and M7-0). This is indicated by the drastically reduced bounce times in the mean centroid trajectory (Figure 8a), such that neither the 5 and 7 μm agglomerates rebound in the normal direction relative to the plate. The standard deviation of the vertical trajectories (Figure 8b) does increase for M3-0, due to the variance in radial trajectory caused by material imperfections. Applying the air does not vary the vertical trajectory behaviour between these constituent particle size differences, however, it suppresses the momentum component of the largest fragment normal to the plate. The air modulates the flow of the largest fragment by the 4-6 ms interval for U_j = 10 and 17 m/s cases, indicated when both the mean and standard deviation of centroid trajectory invert. This spatial information shows how large fragments hold their own trajectory regardless of coflow.

While holding its trajectory, the parent particle rotates with significant angular velocity post-impact. Figure 9(top) shows the snapshots of rotation of the parent

particle after impaction. The snapshots are taken at an interval of 2 ms. The corresponding angular velocity of the particle is shown at the bottom (Figure 9). This rotation corresponds to a significant angular momentum that would likely influence the subsequent trajectory and velocity of ejected fragments (to be presented in a later section). Rotation of fragments should therefore be considered in the analysis de-agglomeration.

4.1.2. Powder Wall Deposition

Figure 10 displays the mean percentage final wall deposition, defined as the ratio of final blocked area (t = SS) and the original single agglomerate blocked area (t = 0 ms). The final blocked area is measured for the earliest steady-state time, t = 150, 100 and 50 ms for U_j = 0, 10 and 17 m/s respectively, shown in final right frame of Figure 5. It is clear that increasing the constituent particle size from 3-7 μm increases the amount of wall deposition irrespective of the degree of applied air . For the free-fall cases, the pseudo-elastic M3-0 collision results in approximately 15% wall deposition whilst up to 60-70% of the M5-0 and M7-0 agglomerates inelastically shatter onto the impaction plate. Applying the air further reduces the measured percentage wall deposition for all cases by transporting broken fragments radially from the point of impact and out of the FOV. A transitional mode from pseudo-elastic to inelastic collision occurs from M3-0 and M3-10 which results in a similar degree of wall deposition. Consistent among both flow-rates and the free-fall case is the similarity between the 5 and 7μm cases compared to the 3μm mannitol, however this is clearly more evident in the free-fall case. This is also consistent with previous observations on blocked area evolution. The standard deviation consistently decreases as air velocity increases, such that at high velocities close to 17 m/s the physical properties of the agglomerate do no affect the degree of final wall deposition.

4.2. Population Distributions - size and characteristic shape

Characterization of the de-agglomerated fragment sizes requires that their shape be considered. All of the fragments that form post-impact, range significantly in their aspect ratios and therefore presentation of a characteristic size would significantly smear out important information on the dynamics of these fragments. In this section the area of each fragment identified is plotted against its respective aspect ratio as a scatter plot.

Figure 11 displays the population distributions for all blocked fragment areas (y-axis, A) against their respective aspect ratio (x-axis, AR). Each plot compares constituent particle size D_{50} = 3, 5 and 7 μm. Moving from left to right shows the effect of U_j = 0, 10, 17 m/s and from top to bottom figures progress forward in time from 1, 3, 7 and 20 ms. Firstly looking at time = 1 ms (top row) for the free-fall cases, initial de-agglomeration is clearly bi-modal in size for all constituent particle sizes (M3-0, M5-0 and M7-0). This is identified with a population of fine 'daughter' fragments less than 0.1 mm^2 and larger 'daughter' remnants, similar in size to the 'parent' agglomerate close to 1 mm^2. The aspect ratio of the larger band is near spherical with AR approximately 1-2, while the smaller band (<0.1 mm^2) includes a significant portion of irregular shapes up to an aspect ratio of 5. This bimodality slightly weakens for increasing air velocity (traversing left to right U_j = 0-17 m/s), and the population of the smaller fragments (<0.1 mm^2) become more concentrated over a narrower region of size and aspect ratio. In terms of shape, the large band increases in aspect ratio range to AR = 0-5 and 0-12 from U_j = 10 and 17 m/s respectively. The significant difference when comparing constituent particle sizes is observed in the fragment shapes, where the 3μm cases (M3-0, M3-10 and M3-17) do not populate shape bands greater than AR = 5 even for increasing U_j. The population size bimodality and shape trends based on air continue with time (see t = 3 ms) until 7 ms after impact. The effect of the air-flow is clear by 7 ms after impact (3rd row)

where the size bimodality has largely dissipated for the U_j = 10 and 17 m/s cases. This occurs due to some local mixing after the air impacts onto the plate. The 3μm cases also drop significantly more in population compared to the 5 and 7 μm counterparts for all size bands when the air is applied. This shows that the fragments are more likely to be airborne rather than attached to the plate, due to the pseudo-elastic collision, induced by stronger agglomerates composed of smaller constituent particles.

4.2.1. Joint Probability Density Functions (PDF)

Instantaneous joint-PDFs of the blocked area, A, and characteristic size, D* (defined as D_{maj}+D_{min})/2) are presented for air velocities U_j = 0, 10 and 17 m/s in Figures 12, 13 and 14 respectively. The constituent particle size increases when traversing from left to right (D_{50} = 3, 5, 7 μm) and time progresses from top to bottom (1, 3, 5, 7 and 20 ms). Small 'daughter' fragments dominate the population globally, shown by a sharp peak for A < 0.1 mm^2 for all constituent particle sizes and air velocities examined.

For the free-fall cases in Figure 12, large remnants of the 'parent' agglomerate typically settle on the plate after impact, indicated by a band with A > 1.3 mm^2 and D* > 1.2 mm remaining from t = 1 ms to t = 20 ms for M3-0 to M7-0. At t = 1 ms, the relationship between blocked area and characteristic size is similar for M3-0 to M7-0 with two discrete bands existing for low A/low D* and high A/high D*. The earliest deterioration of these two bands occurs at t = 7 ms for all constituent particle cases M3-M7. The shape of the joint PDF is not significantly affected by time after impact or by the constituent particle size. With residence time greater than t = 7 ms, a linear relationship between blocked area and characteristic size develops and both A and D* converge to a right-skewed lognormal distribution.

Figures 13 and 14 display the effect of increasing air velocity on the relationship between blocked area and characteristic size. In contrast to the free-fall case, the bimodality between low A/low D* and high A/high D* does not exist and a linear relationship between blocked area and characteristic size exists at t = 1 ms. Air velocity strongly affects the high A/high D* band (A > 1.3 mm^2 and D* > 1.2 mm) such that it is largely dissipated across all cases M3 - M7 by 7 ms. The linear relationship between A and D* is consistently converged with a gradient close to one for M3 at t = 1 ms and the gradient decreases as constituent particle size increases. In Figure 13, this linearity is maintained for M3-10 from t = 1 - 20 ms but weakens with increasing constituent particle size M5 - M7. The main difference is that M3-10 has larger fragments that remain until t = 20 ms, while both M5-10 and M7-10 are very similar across this acquisition window. Figure 14 clearly shows that large fragments occur less for higher constituent particle size when the air velocity is increased to 17m/s. This occurs to such an extent that the high A/high D* bands (A > 1.3 mm^2 and D* > 1.2 mm) are significant reduced immediately after impact (t = 1 ms) for both M5-17 and M7-17. From t = 1 to 7 ms, the decrease in the number of larger fragments with increasing D_{50} remains and the effect eventually converges for all constituent particle cases by t = 20 ms.

4.3. Mean velocity of Fragments

Measurement of the post-impact fragment velocities is critical to fully describe the de-agglomeration process. Three components of velocity are examined here which include the axial (positive in the rebound direction, upward and away from plate), radial (absolute values parallel to plate), and angular velocity (rotational velocity of each particle about out-of-page axis) in order to shed further light on post-impact dynamics. Figure 15 displays the mean and standard deviation of the radial, axial and angular velocity of the fragments as a function of time. The results are pre-

sented for only M3 and M5 cases for the 10 m/s and 17 m/s co-flow. The mean as a function of time is calculated using discrete time bands which fall within: 1-3 ms, 3-5 ms, 5-8 ms, 8-12 ms and 12-16 ms. The mean value measured from each of the time bands are represented on the x-axis and these specific bands are selected to make sure that sufficient data points are used to calculate mean velocity. This is determined here through confirming that the mean values do not change significantly when sampling from more than 100 data points. **The agglomerate velocity before impaction, is $\approx 1.4 \pm 0.2$ m/s, $\approx 4 \pm 0.5$ m/s and $\approx 5.3 \pm 0.5$ m/s for the 0m/s, 10 m/s and 17 m/s coflow, respectively**.

Generally, the results demonstrate the mean radial and axial velocities decrease with time with a generally higher mean radial velocity as compared to the axial component. This is expected as most of the fragments moves in radial direction post-impaction, as observed in Figure 5. The maximum radial velocity is approximately 20**%** of the agglomerate velocity before impaction. The mean radial velocity is higher for the M3-17 and M5-17 cases owing to the higher coflow velocity.

For a constant co-flowing velocity, the radial velocity of M5 is higher as compared to M3. The reason for this is likely attributed to the lower propensity of rebound that is observed for the M5 agglomerates, which results in span-wise (radial) spreading of daughter fragments after impaction. The mean axial velocity is highest for the M3-17 case, owing to the combined effect of higher rebounding of parent agglomerate and higher co-flow. High rebounding results in several fragments moving in the axial direction leading to high axial velocity.

Of interest is to note that owing to the nature of fracture for M5, the radial velocity gradient is slightly sharper in the initial phase (0-4 ms) and shallower in the later phase (4-10 ms) as compared to M3 agglomerates. Initially, the M5 agglomerate breaks instantly (with minimal to no rebound), and the velocity of the de-

agglomerated fragments decay sharply. Later, owing to span-wise spreading, the de-agglomerated fragments of large-daughter agglomerates continue to maintain their velocity for an extended period of time, during which particles are generated. The velocity of these new particles delays the decay of mean velocity to a later phase. This is also evident in Figure 5. For the M3-10 case, the parent agglomerate rebounds and moves out of the measurement volume leaving daughter fragments that do not de-agglomerate further resulting in a gradual decay in mean velocity.

The angular velocity follows a similar trend as those of axial and radial velocity, where it decreases as time progresses. It is observed that for both 10 m/s and 17 m/s co-flow, the angular velocity for M5 agglomerates is higher as compared to M3 agglomerates. The reason for this is not fully understood, however is likely related to the less elastic-like collision for M5 agglomerates. There is also a slight increase in the angular velocity of M3 agglomerates at a later phase in time (10-14ms) due to a dominant contribution from the rotation of the parent agglomerate post-impact. The results indicate a time-dependent effect of powder properties on subsequent de-agglomerate fragment velocity, highlighting the complexity of this problem, which requires further investigation.

In order to shed further light on the complexity of the angular velocity of post impact fragments, figure 16 displays the full probability density function of angular velocity for 10 m/s (left) and 17 m/s co-flow (right). The pdf for M7-17 is not shown due to a lack of samples available to compute a full histogram. A bi-modal distribution for angular velocity is observed for both the M3 and M5 cases, and this bimodality was also observed in size shown earlier. It is observed that most of the particles have a low angular velocity (200-300 rad/s). However, a second peak (shown with an arrow) occurs for M3 and M5 at higher angular velocities. The bi-modal distribution suggests the potential effect of both normal and tangential on the de-agglomeration process. It is possible that the de-agglomeration caused by the shear breakup can

result in higher angular rotation of the daughter de-agglomerates leading to a bi-modal distribution of angular velocity. However, this is cannot be fully substantiated without further investigation. The bimodal distribution is not observed for the M7-10 case as it breaks in the span-wise direction with negligible rebounding of agglomerates. The angular velocity corresponding to the second peak is higher for 17m/s (≈900 rad/s) as compared to 10 m/s (≈700 rad/s), owing to the higher co-flow. The reader should note that the pdf of radial and axial velocity follow expected (log-normal) distributions; and therefore, are not presented here.

5. Summary and Conclusions

Mannitol particles ranging from 3-7 $\boldsymbol{\mu m}$ in median size were used as constituent particles with agglomerate sizes of the order of 1.2-1.5 mm. Through use of advanced in-house image processing techniques, we have isolated the formation of 'daughter' fragments from an agglomerate and characterized their shape, temporal evolution, and overall behaviour. Key variables examined have been the air velocity and constituent particle size. Key conclusions of the paper are as follows:

Increasing the constituent particle size enhances break-up by reducing the fracture strength of the agglomerate, however results in a significantly different behaviour dominated by a higher rate of deposition onto the impaction plate and a radial spreading of particles due to inelastic collision.

Applying air enhances local dispersion and reduces local deposition, due to the introduction of local particle-air mixing in the vicinity of the impaction plate and this applies over all constituent particle sizes. The impact of mixing is more easily observed at later instances in time after initial impact.

Population size and shape distributions shed new light on the morphology of

fragments during de-agglomeration, which identified a bi-modality in fragment sizes due to the isolation of 'parent' from 'daughter' fragments, and this was highly sensitive to applied air. For the free-fall case this bimodality persists over a long interval in time, whereas for the case of 10 and 17m/s, the bimodality dissipates rapidly. Bimodality was also apparent in the probability distribution of angular velocity. Further analysis of velocity of de-agglomerated fragments highlight the transient nature of the break-up process with a decay in velocity as a function of time, and how the change in velocity with time is not necessarily monotonic.

In the context of pharmaceutical dry powder inhalers, these results indicate significant differences in rebound dynamics, deposition behaviour, and shape and size distributions over very slight changes in constituent particle size. The study overarchingly demonstrates how if agglomerates are likely to form, their properties are critical, and small changes in particle size cannot be ignored, particularly with devices that rely on localized impaction for improved de-agglomeration behaviour. Future work could focus on fine particle characterization in such systems, **the role of humidity**, as well as application of these techniques to more complex flows.

6. Acknowledgments

Funding for the research was made possible, in part, by the Australian Research Council through grant DP190101237 and the Food and Drug Administration (United States) through grant 1U01FD006525-01. Views expressed do not necessarily reflect the official policies of the Department of Health and Human Services; nor does any mention of trade names, commercial practices, or organization, imply endorsement by the United States Government.

References

[1] J. Grossman, The evolution of inhaler technology, Journal of Asthma 31 (1) (1994) 55–64. doi:10.3109/02770909409056770.

[2] M. Sanders, Inhalation therapy: an historical review, Primary Care Respiratory Journal: Journal of the General Practice Airways Group 16 (2) (2007) 71–81. doi:10.3132/pcrj.2007.00017.

[3] H. W. Frijlink, A. H. De Boer, Dry powder inhalers for pulmonary drug delivery, Expert Opinion on Drug Delivery 1 (1) (2004) 67–86. doi:10.1517/17425247.1.1.67.

[4] Y. Javadzadeh, S. Yaqoubi, Therapeutic nanostructures for pulmonary drug delivery, in: E. Andronescu, A. M. Grumezescu (Eds.), Nanostructures for Drug Delivery, Micro and Nano Technologies, Elsevier, 2017, Ch. 20, pp. 619–638. doi:10.1016/B978-0-323-46143-6.00020-8.

[5] A. Kourmatzis, S. Cheng, H.-K. Chan, Airway geometry, airway flow, and particle measurement methods: implications on pulmonary drug delivery, Expert Opinion on Drug Delivery 15 (3) (2018) 271–282. doi:10.1080/17425247.2018.1406917.

[6] N. Islam, E. Gladki, Dry powder inhalers (DPIs)–a review of device reliability and innovation, International Journal of Pharmaceutics 360 (1) (2008) 1–11. doi:10.1016/j.ijpharm.2008.04.044.

[7] L. Borgström, T. Bengtsson, E. Derom, R. Pauwels, Variability in lung deposition of inhaled drug, within and between asthmatic patients, with a pMDI and a dry powder inhaler, turbuhaler®, International Journal of Pharmaceutics 193 (2) (2000) 227–230. doi:10.1016/S0378-5173(99)00341-5.

[8] M. J. Telko, A. J. Hickey, Dry powder inhaler formulation, Respiratory Care 50 (9) (2005) 1209–1227.

[9] S. Adi, H. Adi, H.-K. Chan, W. H. Finlay, Z. Tong, R. Yang, A. Yu, Agglomerate strength and dispersion of pharmaceutical powders, Journal of Aerosol Science 42 (4) (2011) 285–294. doi:10.1016/j.jaerosci.2011.02.002.

[10] F. Nicklasson, G. Alderborn, Analysis of the compression mechanics of pharmaceutical agglomerates of different porosity and composition using the adams and kawakita equations, Pharmaceutical Research 17 (8) (2000) 949–954. doi:10.1023/A:1007575120817.

[11] D. G. Bika, M. Gentzler, J. N. Michaels, Mechanical properties of agglomerates, Powder Technology 117 (1) (2001) 98–112. doi:10.1016/S0032-5910(01)00318-7.

[12] P. Begat, D. A. V. Morton, J. N. Staniforth, R. Price, The cohesive-adhesive balances in dry powder inhaler formulations i: Direct quantification by atomic force microscopy, Pharmaceutical Research 21 (9) (2004) 1591–1597. doi:B:PHAM.0000041453.24419.8a.

[13] J. Yang, C.-Y. Wu, M. Adams, Numerical modelling of agglomeration and deagglomeration in dry powder inhalers: A review, Current Pharmaceutical Design 21 (40) (2015) 5915–5922.

[14] N. Islam, M. J. Cleary, Developing an efficient and reliable dry powder inhaler for pulmonary drug delivery–a review for multidisciplinary researchers, Medical Engineering & Physics 34 (4) (2012) 409–427. doi:10.1016/j.medengphy.2011.12.025.

[15] n. Sumby, n. Slater, n. Atkins, n. Prime, Review of dry powder inhalers,

Advanced Drug Delivery Reviews 26 (1) (1997) 51–58. doi:10.1016/s0169-409x(97)00510-3.

[16] W. H. Finlay, Dry-powder inhalers, in: W. H. Finlay (Ed.), The Mechanics of Inhaled Pharmaceutical Aerosols (Second Edition), Academic Press, 2019, Ch. 9, pp. 213–262. doi:10.1016/B978-0-08-102749-3.00009-9.

[17] A. Voss, W. H. Finlay, Deagglomeration of dry powder pharmaceutical aerosols, International Journal of Pharmaceutics 248 (1) (2002) 39–50. doi:10.1016/S0378-5173(02)00319-8.

[18] W. Wong, D. F. Fletcher, D. Traini, H.-K. Chan, J. Crapper, P. M. Young, Particle aerosolisation and break-up in dry powder inhalers: Evaluation and modelling of the influence of grid structures for agglomerated systems, Journal of Pharmaceutical Sciences 100 (11) (2011) 4710–4721. doi:10.1002/jps.22663.

[19] G. Calvert, M. Ghadiri, R. Tweedie, Aerodynamic dispersion of cohesive powders: A review of understanding and technology, Advanced Powder Technology 20 (1) (2009) 4–16. doi:10.1016/j.apt.2008.09.001.

[20] M. S. Coates, D. F. Fletcher, H.-K. Chan, J. A. Raper, Effect of design on the performance of a dry powder inhaler using computational fluid dynamics. part 1: Grid structure and mouthpiece length, Journal of Pharmaceutical Sciences 93 (11) (2004) 2863–2876. doi:10.1002/jps.20201.

[21] M. S. Coates, H.-K. Chan, D. F. Fletcher, J. A. Raper, Influence of air flow on the performance of a dry powder inhaler using computational and experimental analyses, Pharmaceutical Research 22 (9) (2005) 1445–1453. doi:10.1007/s11095-005-6155-x.

[22] M. S. Coates, H.-K. Chan, D. F. Fletcher, J. A. Raper, Effect of design on the performance of a dry powder inhaler using computational fluid dynamics. part

2: Air inlet size, Journal of Pharmaceutical Sciences 95 (6) (2006) 1382–1392. doi:10.1002/jps.20603.

[23] R. Han, G. Papadopoulos, B. J. Greenspan, Investigation of powder dispersion inside a SPIROS® dry powder inhaler using particle image velocimetry, Powder Technology 125 (2) (2002) 266–278. doi:10.1016/S0032-5910(01)00515-0.

[24] X. Kou, S. T. Wereley, P. W. S. Heng, L. W. Chan, M. T. Carvajal, Powder dispersion mechanisms within a dry powder inhaler using microscale particle image velocimetry, International Journal of Pharmaceutics 514 (2) (2016) 445–455. doi:10.1016/j.ijpharm.2016.07.040.

[25] Z. B. Tong, R. Y. Yang, A. B. Yu, S. Adi, H. K. Chan, Numerical modelling of the breakage of loose agglomerates of fine particles, Powder Technology 196 (2) (2009) 213–221. doi:10.1016/j.powtec.2009.08.001.

[26] C. Thornton, M. T. Ciomocos, M. J. Adams, Numerical simulations of agglomerate impact breakage, Powder Technology 105 (1) (1999) 74–82. doi:10.1016/S0032-5910(99)00120-5.

[27] J. Yang, C.-Y. Wu, M. Adams, DEM analysis of the effect of particle–wall impact on the dispersion performance in carrier-based dry powder inhalers, International Journal of Pharmaceutics 487 (1) (2015) 32 – 38. doi:https://doi.org/10.1016/j.ijpharm.2015.04.006.

[28] W. Wong, D. F. Fletcher, D. Traini, H.-K. Chan, J. Crapper, P. M. Young, Particle aerosolisation and break-up in dry powder inhalers 1: Evaluation and modelling of venturi effects for agglomerated systems, Pharmaceutical Research 27 (7) (2010) 1367–1376. doi:10.1007/s11095-010-0128-4.

[29] A. Kourmatzis, P. X. Pham, A. R. Masri, A two-angle far-field microscope imag-

ing technique for spray flows, Measurement Science and Technology 28 (3) (2017) 035302. doi:10.1088/1361-6501/aa5525.

[30] A. Lowe, A. Kourmatzis, A. R. Masri, Turbulent spray flames of intermediate density: Stability and near-field structure, Combustion and Flame 176 (2017) 511–520. doi:http://dx.doi.org/10.1016/j.combustflame.2016.10.024.

[31] J. T. Kashdan, J. S. Shrimpton, A. Whybrew, Two-phase flow characterization by automated digital image analysis. part 2: Application of PDIA for sizing sprays, Particle & Particle Systems Characterization 21 (1) (2004) 15–23. doi:10.1002/ppsc.200400898.

7. Tables

Table I: Spray drying conditions for mannitol (denoted with coefficient M) constituent particles of different sizes 3, 5, 7 μm (M3-M7).

	M3	M5	M7
Feed Conc. (mg/mL)	4	10	18
Feed rate (mL/min)	3.8 (11%)	4.1 (12%)	8 (20%)
Humidity (%)	33	33	33
Inlet Temp. (°C)	140	140	140
Outlet Temp. (°C)	85	87	87
D_{50} (μm)	2.92	4.96	6.77
Approximate Density (Kg/m^3)	554.6	360.2	374.8

Table II: Initial Conditions - Single Agglomerate Impaction Channel.

CASE	M3-0	M5-0	M7-0	M3-10	M5-10	M7-10	M3-17	M5-17	M7-17
Air Jet Loading (g/min)	0	0	0	72	72	72	123	123	123
Air Jet Velocity (m/s)	0	0	0	10	10	10	17	17	17
Air Jet Re	0	0	0	6617	6617	6617	11250	11250	11250
D_{50} (μm)	2.92	4.96	6.77	2.92	4.96	6.77	2.92	4.96	6.77

8. Figures

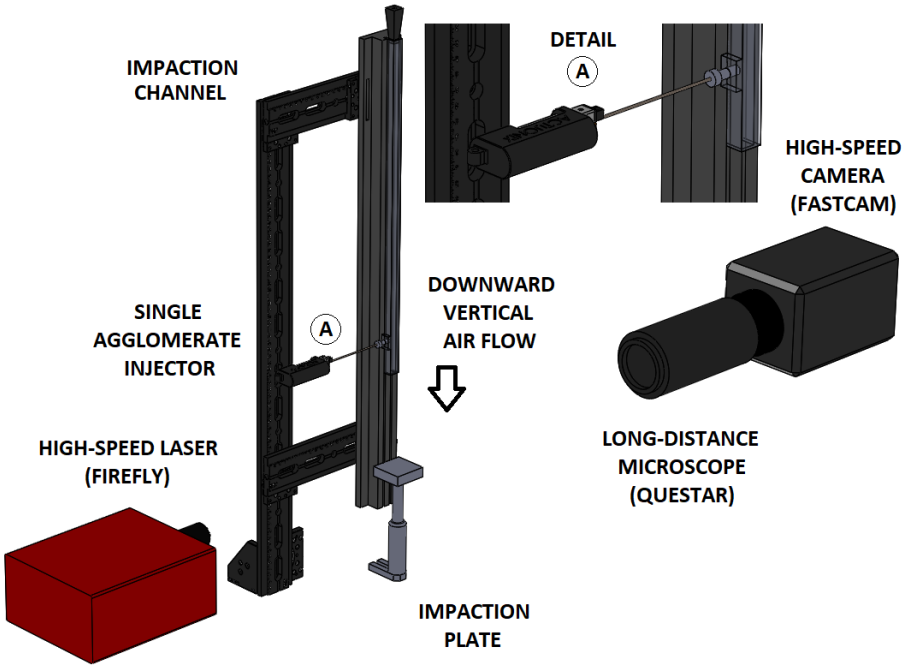

Fig. 1: Single agglomerate impaction channel for high-speed microscopic backlit imaging measurements. Dimensions defined in Section 2.2.

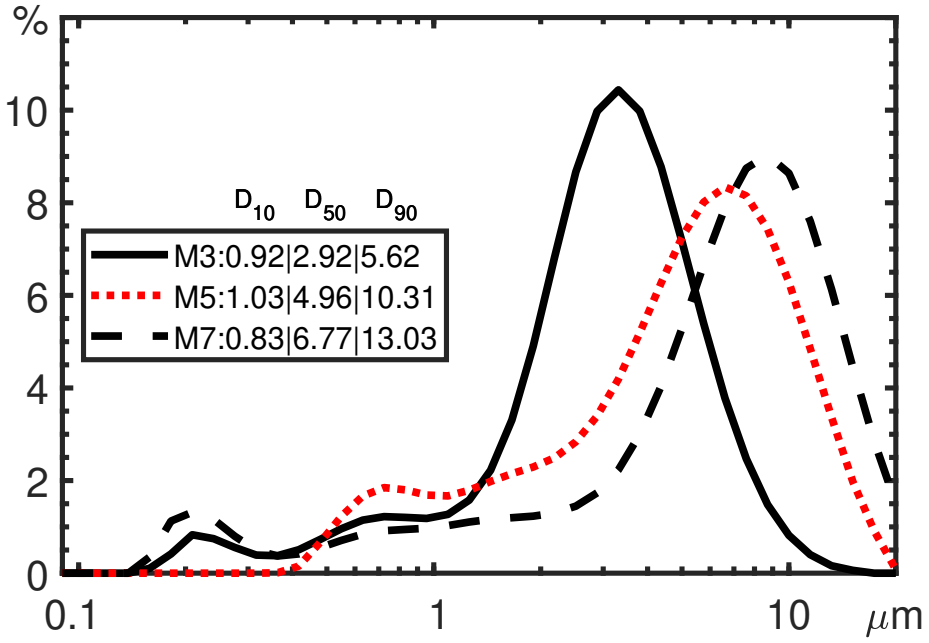

Fig. 2: Population size distributions by volume for mannitol powders approximated to 3, 5 and 7 $\boldsymbol{\mu}$m (M3 solid black, M5 dotted red and M7 dashed black respectively) using a wet Malvern particle sizer. The legend provides the corresponding extracted D_{10}, D_{50} and D_{90} values.

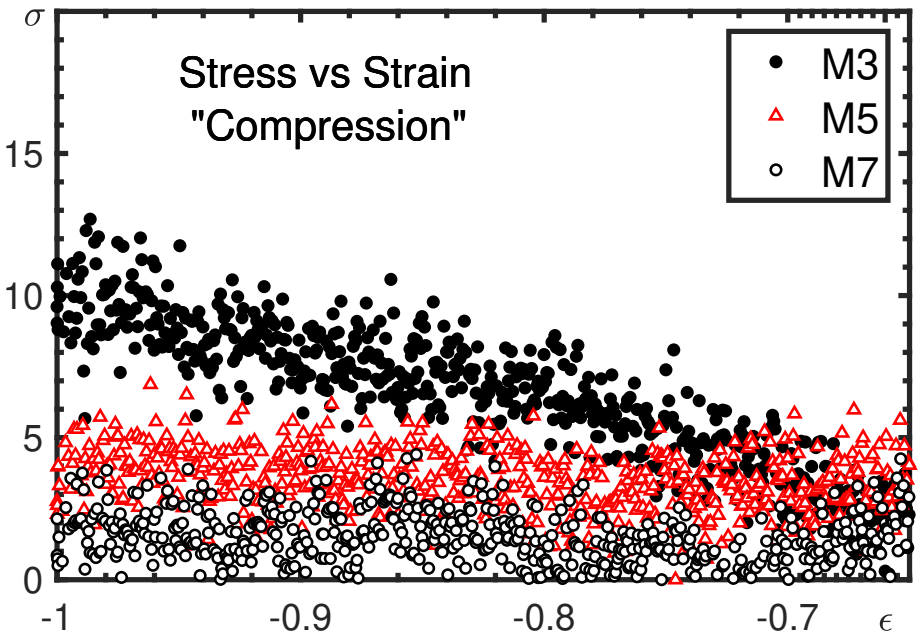

Fig. 3: Stress ($\boldsymbol{\sigma}$, kPa) against strain ($\boldsymbol{\epsilon}$) scatter relationship for 1.2-1.5 mm diameter agglomerates consisting of 3, 5 and 7 $\boldsymbol{\mu}$m mannitol (M3, M5, M7 respectively). Measurements were made with an electro-mechanical instron (low-load 0.5kN), where the strain rate was 3 $\boldsymbol{\mu}$m per second. Data points are plotted for five compression tests per constituent particle size case.

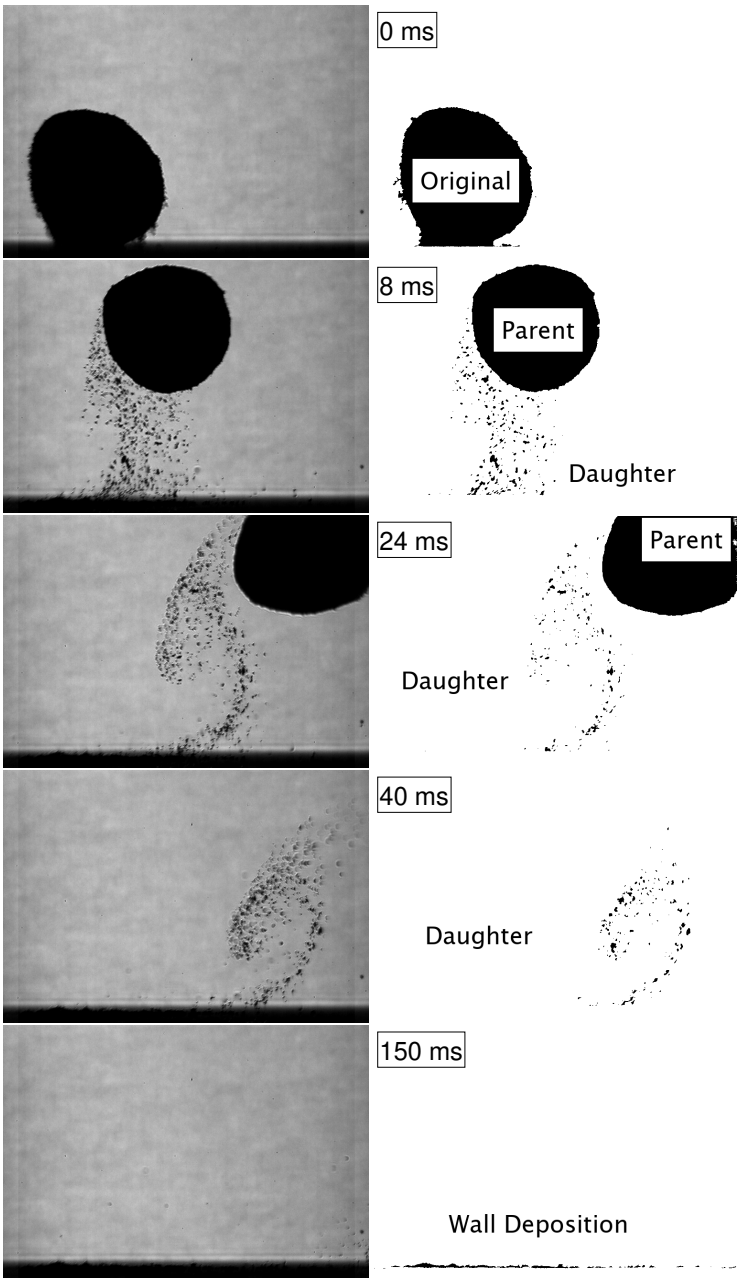

Fig. 4: Backlit image sequence of 'free-fall' de-agglomeration for a diameter, D = 1.2-1.5 mm, where the constituent mannitol particles have a D_{50} = 3μm (M3-0). Raw images (left) and corresponding processed images (right); time progresses from top to bottom and t = 0 ms is defined as the first instance the surface of the agglomerate contacts the impaction plate.

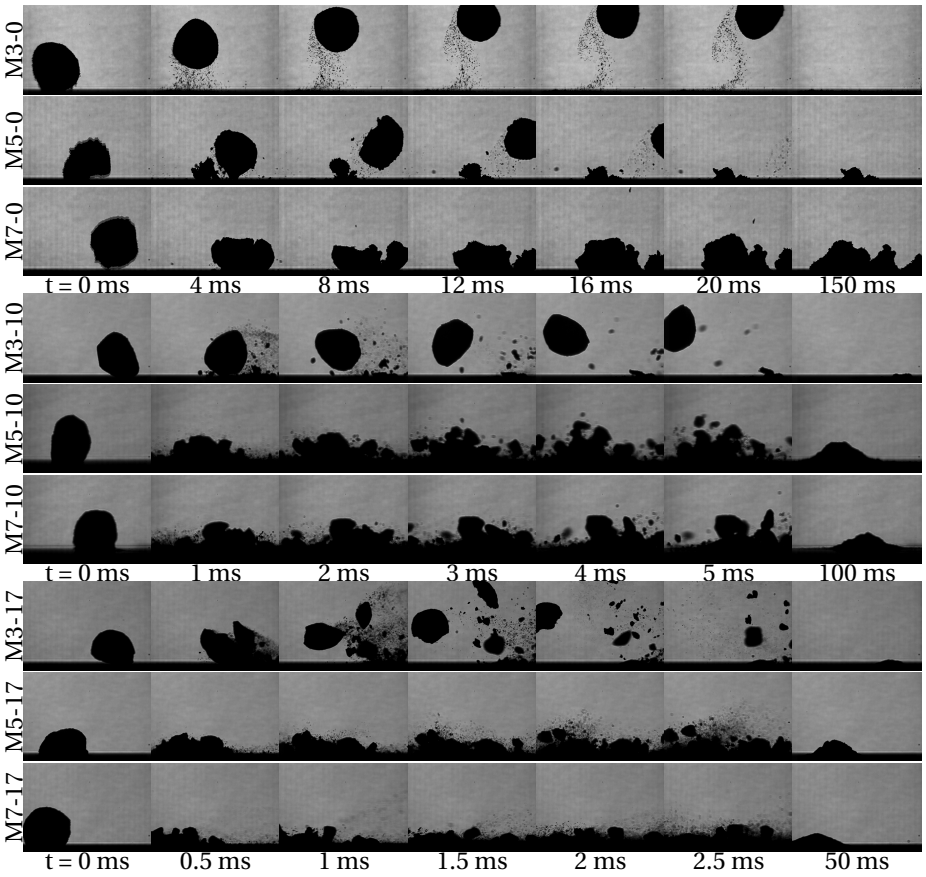

Fig. 5: Backlit image sequences of de-agglomeration for single agglomerates (D=1.2-1.5mm) of mannitol where the air velocity, U_j is varied 0 m/s, 10 m/s and 17 m/s (refer to Table II). Time progresses from left to right; t = 0 ms is defined as the first instance the surface of the agglomerate contacts the impaction plate and the last frame is the steady-state time, t = SS. For each air velocity, the constituent particle size is varied to approximately 3 μm (M3), 5 μm (M5) and 7 μm (M7).

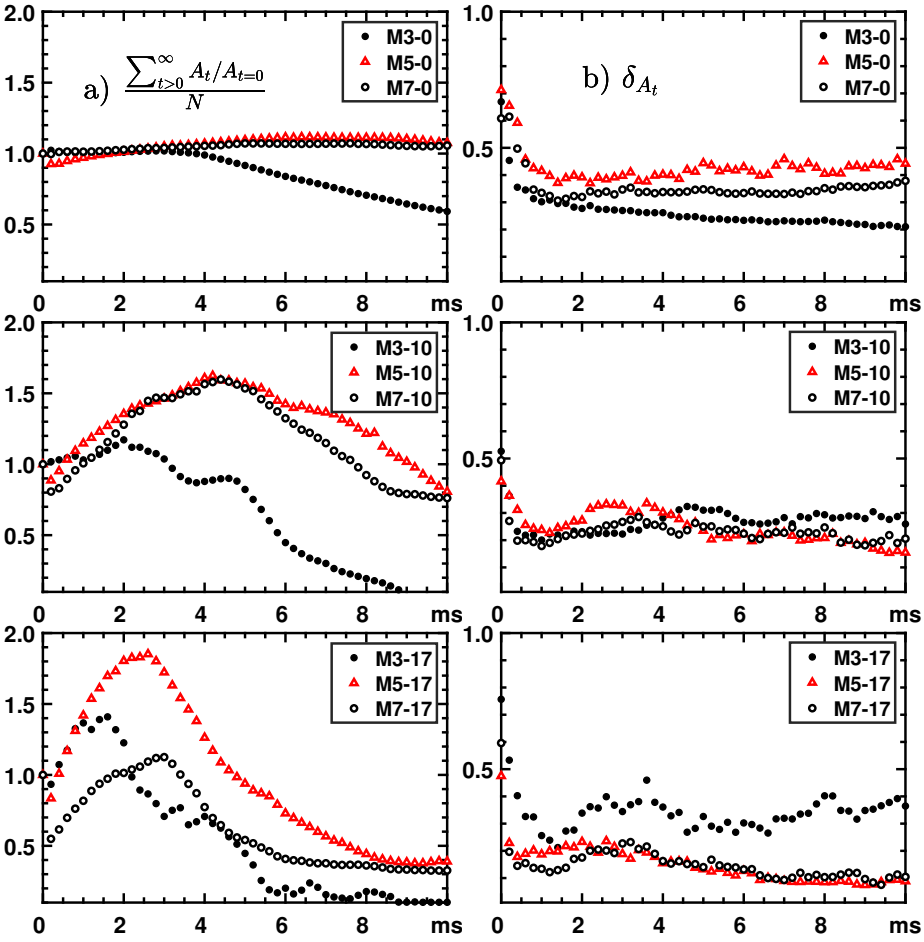

Fig. 6: Temporal evolution of the a) normalized area (mean total instantaneous blocked area normalized by the original agglomerate blocked area) and b) one standard deviation of the instantaneous blocked areas. Each plot compares characteristics based on D_{50} and the air velocity ranges from 0, 10 and 17 m/s (top to bottom respectively).

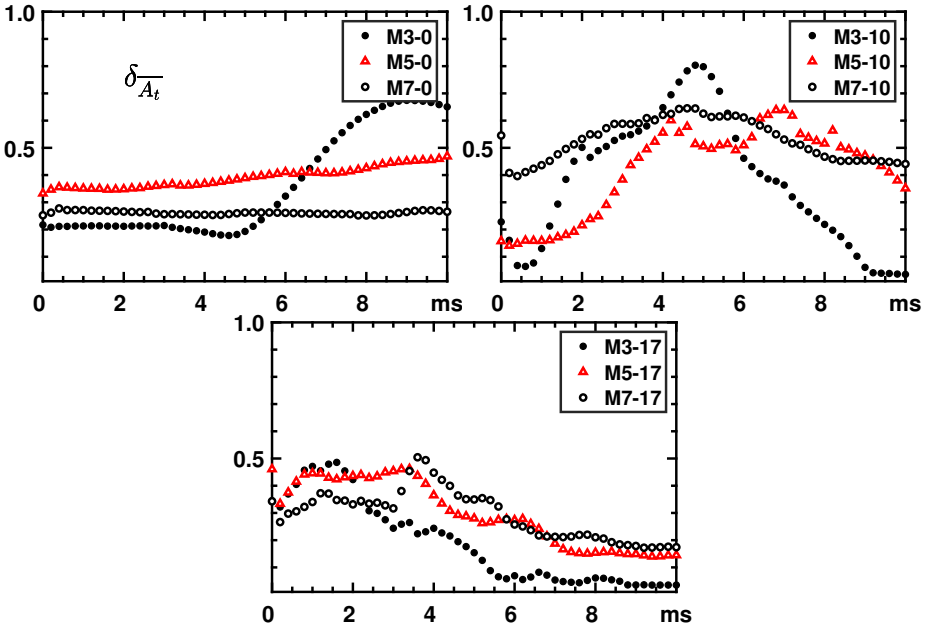

Fig. 7: Temporal evolution of one standard deviation of the instantaneous mean blocked area. Each plot compares characteristics based on D_{50} and the air velocity ranges from 0, 10 and 17 m/s.

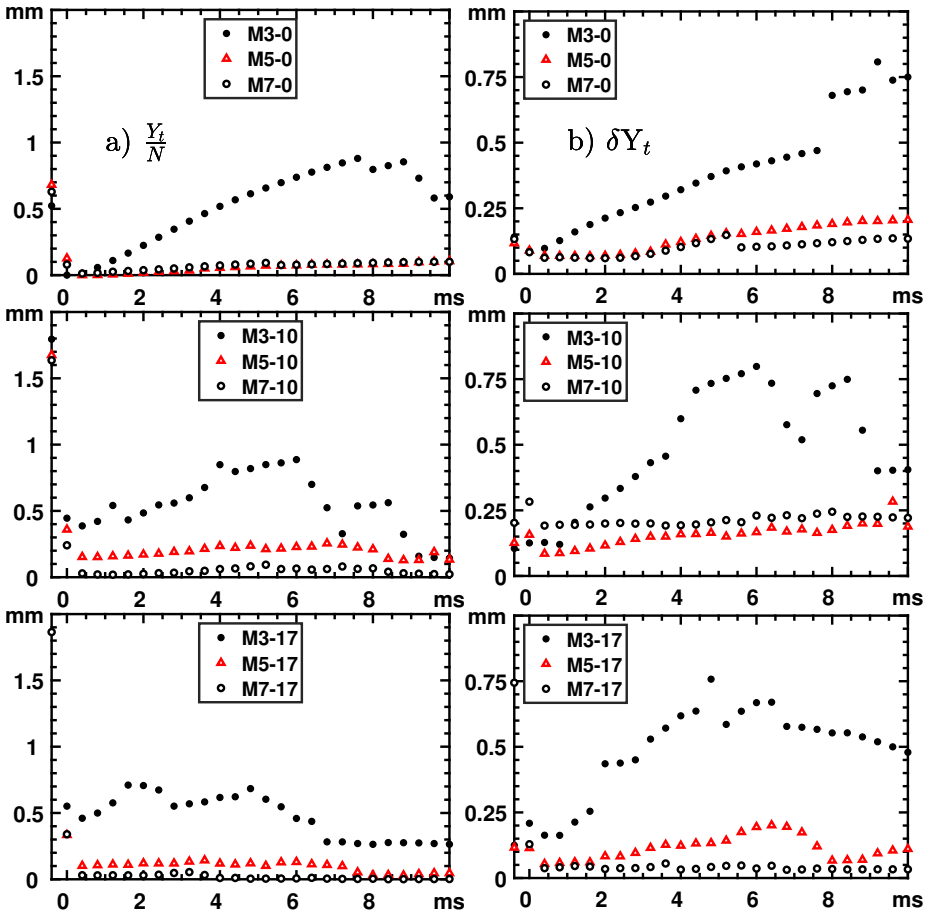

Fig. 8: Temporal centroid vertical trajectory a) mean Y_t and b) standard deviation δY_t, for the single largest mannitol agglomerate/fragment ('parent') in the acquisition field of view. Time, t = 0 ms is defined as the first instance the surface of the agglomerate contacts the impaction plate and each plot compares characteristics based on D_{50} and the air velocity ranges from 0, 10 and 17 m/s (top to bottom respectively).

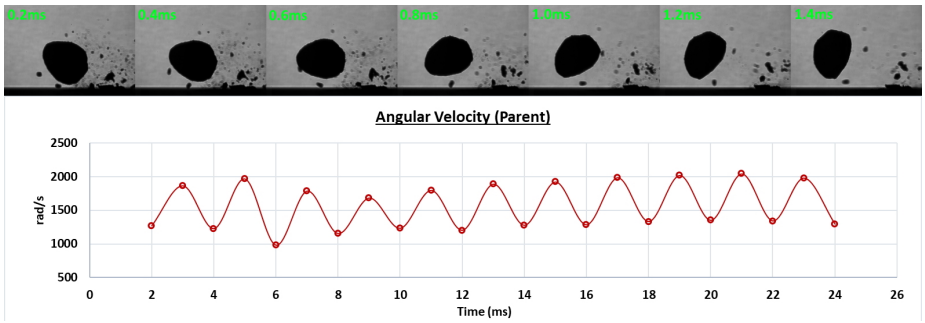

Fig. 9: Temporal evolution of angular velocity. The top figure shows the snapshots of angular movement of parent particle. The bottom figure shows the corresponding angular velocity as a function of time.

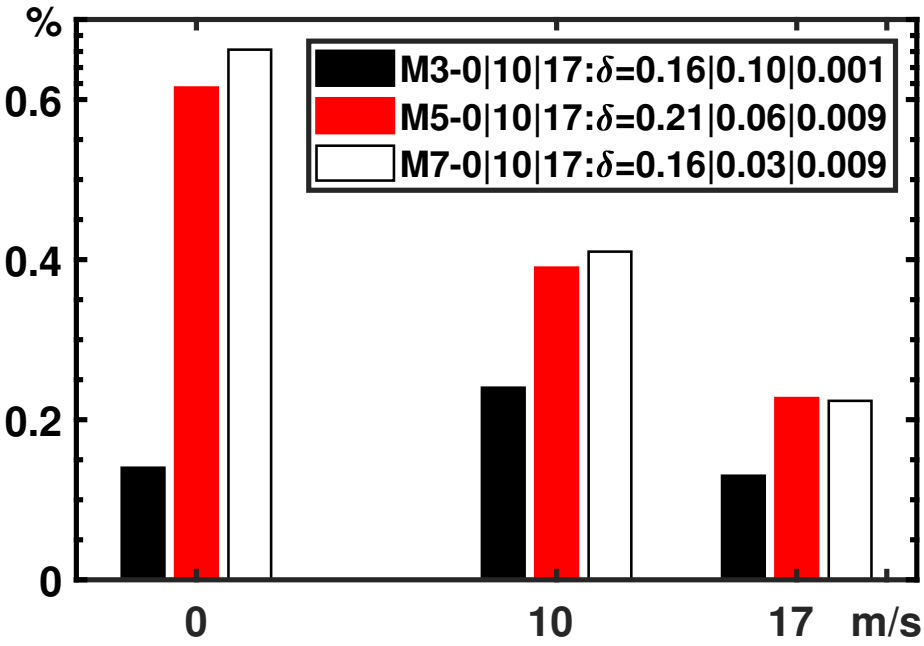

Fig. 10: Percentage final wall deposition over the original agglomerate blocked area, comparing effects of D_{50} from 3-7μm (M3 (black), M5 (red), M7 (white)) for air velocity ranging from 0, 10 and 17 m/s. The legend provides a single standard deviation, δ, of the final wall deposition blocked area; for example, δ = 0.16, 0.1 and 0.001 for M3-0, M3-10 and M3-17 respectively.

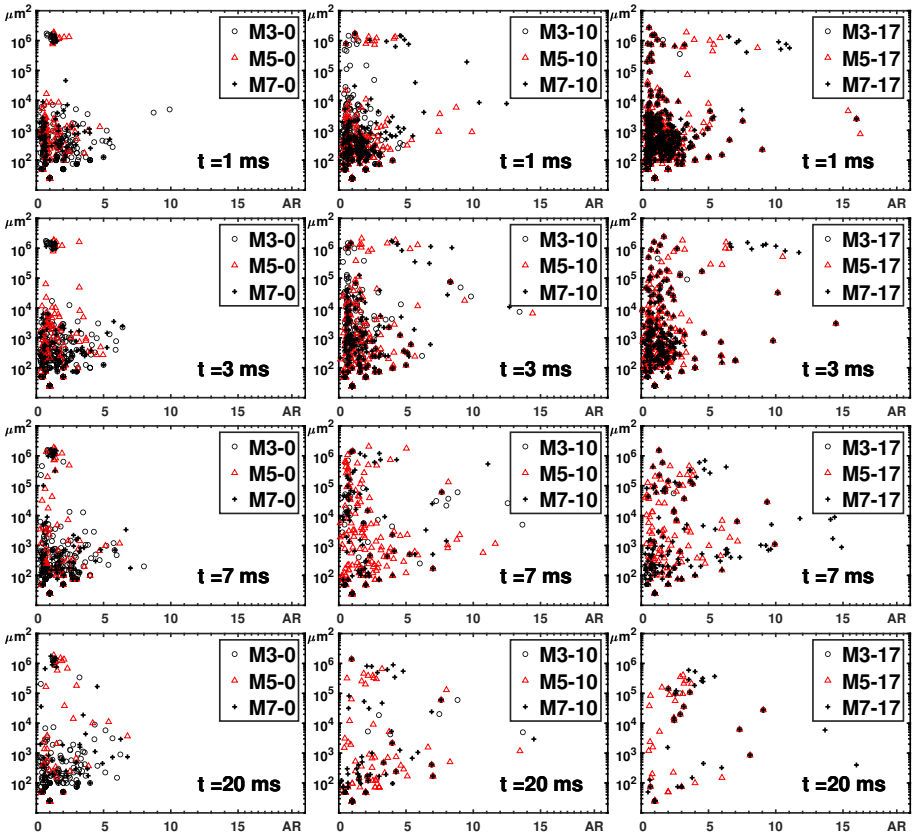

Fig. 11: Population distribution of fragment blocked area (A) against relative aspect ratio (AR), comparing constituent particle size D_{50} = 3, 5 and 7 μm. Left to right comparing U_j = 0, 10, 17 m/s and top to bottom, comparing 1, 3, 7 and 20 ms time instances. The original agglomerate ranges in size from $A_{t<0}$ = 1.3 - 1.77 x 10^6 μm^2.

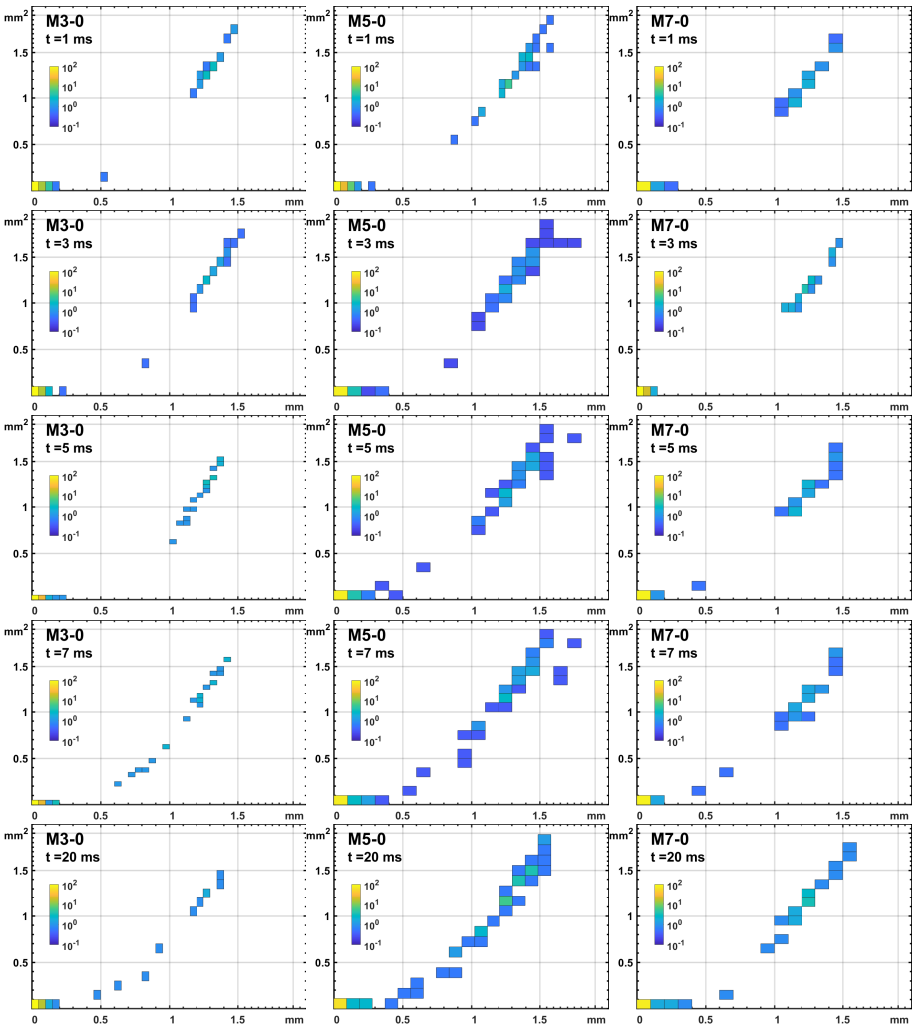

Fig. 12: Joint PDF of blocked area, A (y-axis), and characteristic size, D^* (x-axis, defined as $(D_{maj}+D_{min})/2$) for air velocity 0 m/s and comparing constituent particle size D_{50} = 3, 5 and 7 μm (columns 1-3 respectively). Time progresses top to bottom, comparing 1, 3, 5, 7 and 20 ms instances. The original agglomerate ranges in $A_{t<0}$ = 1.3 - 1.77 mm^2 and $D_{t<0}$ = 1.2 - 1.5 mm.

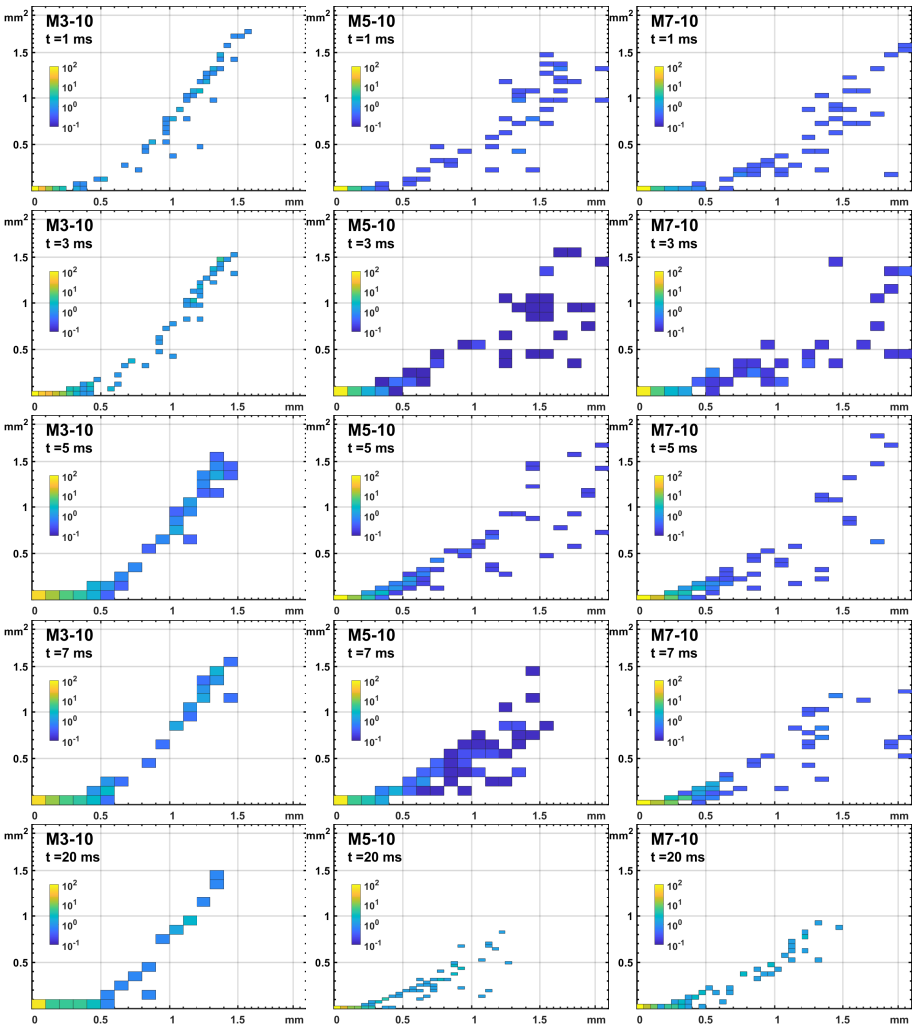

Fig. 13: Joint PDF of blocked area, A (y-axis), and characteristic size, D^* (x,axis, defined as $(D_{maj}+D_{min})/2$) for air velocity 10 m/s and comparing constituent particle size D_{50} = 3, 5 and 7 μm (columns 1-3 respectively). Time progresses top to bottom, comparing 1, 3, 5, 7 and 20 ms instances. The original agglomerate ranges in $A_{t<0}$ = 1.3 - 1.77 mm^2 and $D_{t<0}$ = 1.2 - 1.5 mm.

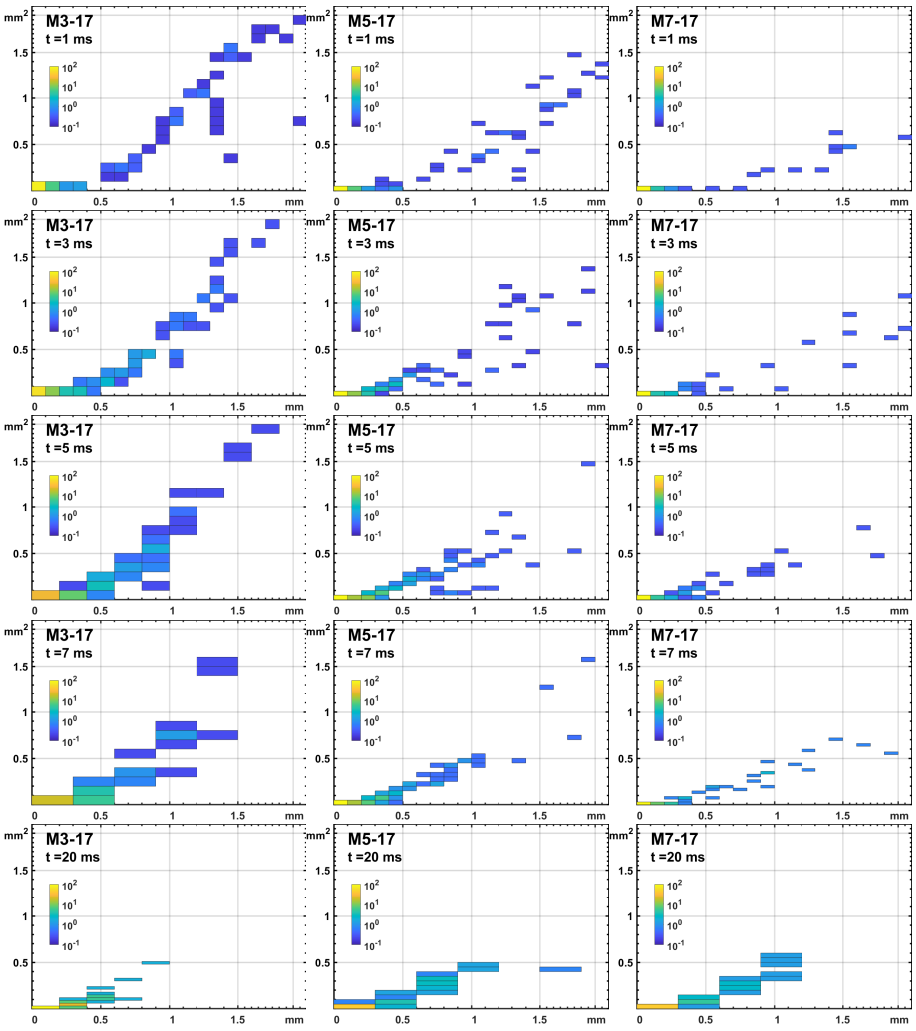

Fig. 14: Joint PDF of blocked area, A (y-axis), and characteristic size, D^* (x-axis, defined as $(D_{maj}+D_{min})/2$) for air velocity 17 m/s and comparing constituent particle size D_{50} = 3, 5 and 7 μm (columns 1-3 respectively). Time progresses top to bottom, comparing 1, 3, 5, 7 and 20 ms instances. The original agglomerate ranges in $A_{t<0}$ = 1.3 - 1.77 mm^2 and $D_{t<0}$ = 1.2 - 1.5 mm.

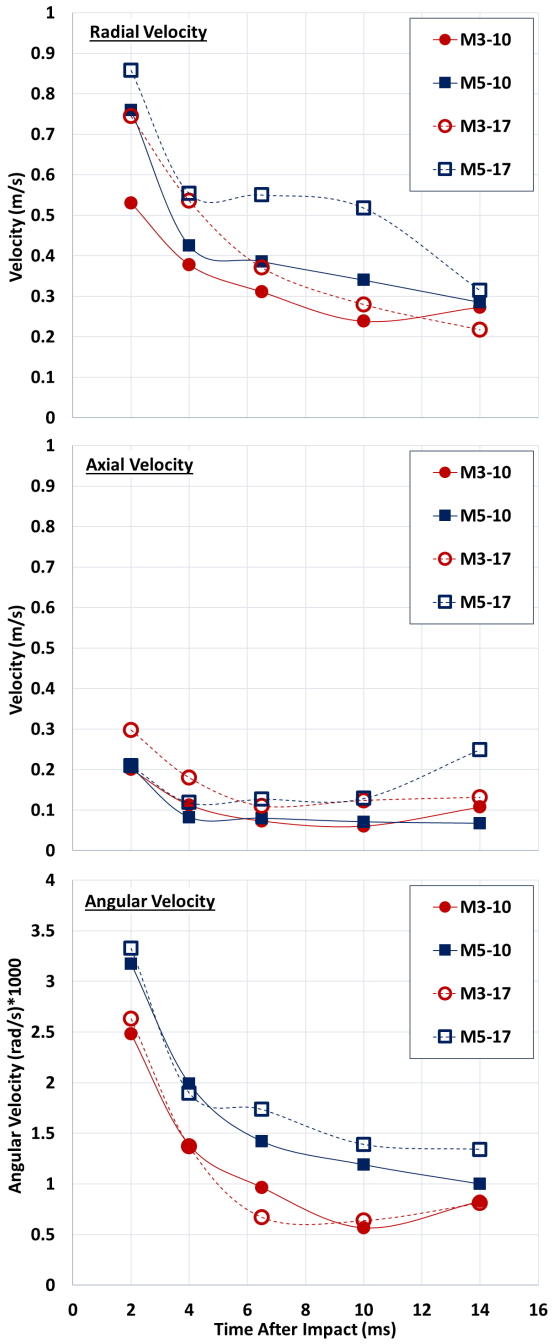

Fig. 15: The mean of radial, axial and angular velocity of M3 and M5. Presented here as a function of time after impaction.

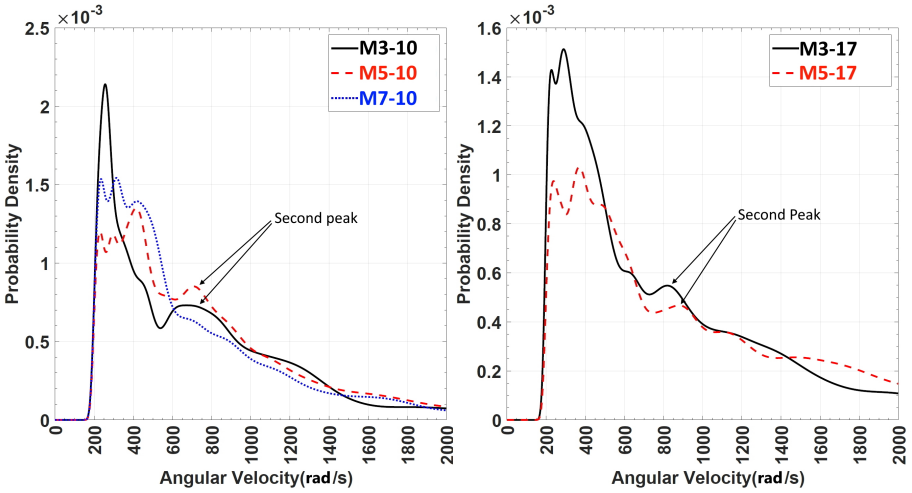

Fig. 16: PDF of angular velocity of fragments for M3, M5 and M7 at air velocities of 10 m/s (left) and 17 m/s (right).